Journal of Computational Physics 227 (2008) 8417–8436

Contents lists available at ScienceDirect

Journal of Computational Physics

journal homepage: www.elsevier.com/locate/jcp

Comparisons of weakly compressible and truly incompressible algorithms for the SPH mesh free particle method

E.-S. Lee [a], C. Moulinec [b], R. Xu [c], D. Violeau [a,*], D. Laurence [c], P. Stansby [c]

[a] EDF R&D - LNHE, 6 quai Watier, 78400 Chatou, France
[b] STFC Daresbury Laboratory, Daresbury, Warrington WA4 4AD, England
[c] School of Mechanical, Aerospace and Civil Engineering, The University of Manchester, Manchester, UK, M60 1QD, England

ARTICLE INFO

Article history:
Received 21 December 2006
Received in revised form 29 January 2008
Accepted 9 June 2008
Available online 19 June 2008

Keywords:
SPH
Incompressible flows
Pressure Poisson equation
Lagrangian modelling

ABSTRACT

In the smoothed particle hydrodynamics (SPH) discretisation method for the Navier–Stokes equations the most widespread method to solve for pressure and mass conservation is the weakly compressible assumption (WCSPH). This includes hydraulics applications and leads to some drawbacks such as severe artificial pressure fluctuations and a limitation to very small time steps related to the WCSPH Mach number and explicit method. This paper presents comparisons of a semi-implicit and truly incompressible SPH (ISPH) algorithm with the classical WCSPH method, showing how some of the problems encountered in WCSPH have been resolved by using ISPH to simulate incompressible flows. Mathematical models are presented before describing SPH formalism. Several standard boundary conditions are introduced and special attention is given to tracking the surface particles. The lid-driven cavity flow ($Re = 400$ and 1000) is performed as a benchmarking test. A bluff body test case (a square cylinder in a closed channel, $Re_d = 20$ and 100 based on the cylinder diameter) shows that pressure fields extracted from WCSPH are very unreliable whereas ISPH predict pressures and forces in closer agreement with classical finite volume CFD methods. Dam-breaking cases, with dry or wet beds downstream, are then presented to highlight free-surface flow and rapid dynamics effects. The WCSPH and ISPH results are generally verified with reference data from experiment and/or another numerical method. All the comparisons show improvement with ISPH and good agreement in general.

1. Introduction

Smoothed particle hydrodynamics (SPH) is a fully Lagrangian method, which does not require the use of any mesh. It was originally invented to simulate astrodynamics [13]. Since then the use of SPH has expanded in many areas of solid and fluid dynamics (involving large deformations, impacts, free-surface and multiphase flows). A major advantage of SPH over Eulerian methods is the ability to capture very complex interfaces without any special front tracking treatment. When modelling incompressible flows, traditional SPH solvers resort to a weakly compressible approach (hereafter referred to as WCSPH). The advantage is that it is easy to programme because the pressure is obtained from an algebraic thermodynamic equation [14] and diffusion terms are treated as explicit. However, some drawbacks appear. Firstly, WCSPH requires a very small time step associated with a numerical speed of sound which is at least 10 times higher than the maximum of velocity. Secondly, small density errors always remain causing significant non-physical pressure fluctuations which can yield numerical instability. Circumventing those problems can be achieved by using truly incompressible SPH (hereafter referred to as ISPH).

* Corresponding author.
E-mail address: damien.violeau@edf.fr (D. Violeau).

0021-9991/$ - see front matter © 2008 Elsevier Inc. All rights reserved.
doi:10.1016/j.jcp.2008.06.005

Pressure and viscous forces are treated separately, the pressure being calculated by enforcing a divergence-free velocity field [4]. The pressure is thus no longer a dependent variable but is computed from a pressure Poisson equation.

The work presented here uses the SPARTACUS-2D code as a starting point, a code initially developed at the "*Laboratoire National d'Hydraulique et d'Environnement*" of EDF (*Electricité de France*) since 1998 by Violeau and Issa (see [7]) with the WCSPH formulation.

In this paper, weakly compressible and truly incompressible algorithms are introduced followed by the SPH formulations, with free-surface and solid wall boundary conditions. Test cases consist of a 2-D lid-driven cavity flow, a flow around a bluff body, and finally several dam-break applications.

2. Governing equations and numerical schemes

In this section, the numerical methods used to solve the equations for incompressible flows of Newtonian fluids are described; SPH notations and tools are introduced in Section 3.

2.1. Weakly compressible algorithm

A classical method which solves weakly compressible equations in primitive variables (density ρ, velocity $\mathbf{u}$) is presented in this subsection. As a result, the Lagrangian Reynolds-Averaged Navier–Stokes equations read

$$\frac{1}{\rho}\frac{\mathrm{d}\rho}{\mathrm{d}t} + \nabla\cdot\bar{\mathbf{u}} = 0 \tag{1}$$

$$\frac{\mathrm{d}\bar{\mathbf{u}}}{\mathrm{d}t} = -\frac{1}{\rho}\nabla\bar{p} + \nabla\cdot(\nu_{\mathrm{E}}\nabla\bar{\mathbf{u}}) + \mathbf{F}^{\mathrm{e}} \tag{2}$$

where ρ is the density, $\bar{\mathbf{u}}$ is the Reynolds averaged velocity vector, t the time, $\bar{p}$ the Reynolds-averaged pressure, $\nu_{\mathrm{E}}=\nu+\nu_{\mathrm{T}}$ the effective viscosity, ν being the kinematic viscosity and ν_{T} the turbulent viscosity, and $\mathbf{F}^{\mathrm{e}}$ an external force such as gravity for instance. Every vector quantity is written in bold. "∇" and "$\nabla\cdot$" are respectively gradient and divergence operators. The overstrike bar indicates Reynolds averaging.

The system composed of Eqs. (1) and (2) is closed by a relation between ρ and $\bar{p}$ taking the form of an appropriate equation of state for water:

$$\bar{p} = \frac{\rho_0 c_0^2}{\gamma}\left(\left(\frac{\rho}{\rho_0}\right)^{\gamma} - 1\right) \tag{3}$$

where $\gamma = 7$, ρ_0 is a reference density and c_0 is a numerical speed of sound which is normally taken 10 times higher than the maximum fluid velocity in order to reduce the density fluctuation down to 1% [14]. Due to the power coefficient γ, small density fluctuations lead to large pressure fluctuations but the noise induced in the pressure field does not generally contaminate the flow evolution. This approach tends to keep the particle distances roughly constant by imposing a repelling force to a pair of particles when they come too close to each other.

The scheme is first order and fully explicit in time. The following equations give the sequence of the WCSPH algorithm. The velocity is calculated as

$$\bar{\mathbf{u}}^{n+1} = \bar{\mathbf{u}}^{n} + \left(-\frac{1}{\rho}\nabla\bar{p}^{n} + \nabla\cdot(\nu_{\mathrm{E}}\nabla\bar{\mathbf{u}}^{n}) + \mathbf{F}^{\mathrm{e}}\right)\Delta t \tag{4}$$

where superscripts n and $n+1$ indicate, respectively, previous and present time steps and Δt is the numerical time step.

Position and density are updated at the next time step by

$$\mathbf{r}^{n+1} = \mathbf{r}^{n} + \bar{\mathbf{u}}^{n+1}\Delta t, \quad \rho^{n+1} = \rho^{n} - \rho^{n}(\nabla\cdot\bar{\mathbf{u}}^{n+1})\Delta t \tag{5}$$

Finally, the pressure is obtained from Eq. (3) with the updated density.

2.2. Truly incompressible algorithm

The truly incompressible approach dealing with pressure and velocity as primitive variables is presented in this section. The density is constant and Eq. (1) reduces to

$$\nabla\cdot\bar{\mathbf{u}} = 0 \tag{6}$$

The classical projection method [2,21] is used to solve the velocity–pressure coupling problem. The discretised form of Eq. (2) is split into two parts: the first being the prediction step based on viscous and gravity forces:

$$\frac{\bar{\mathbf{u}}^{*} - \bar{\mathbf{u}}^{n}}{\Delta t} = \nabla\cdot(\nu_{\mathrm{E}}\nabla\bar{\mathbf{u}}^{n}) + \mathbf{F}^{\mathrm{e}} \tag{7}$$

and the latter the correction step based on pressure force:

$$\frac{\bar{\mathbf{u}}^{n+1} - \bar{\mathbf{u}}^{*}}{\Delta t} = -\frac{1}{\rho}\nabla\bar{p}^{n+1} \tag{8}$$

where $\bar{\mathbf{u}}^*$ is an auxiliary velocity. In the prediction step, Eq. (7) can be rewritten as

$$\bar{\mathbf{u}}^* = \bar{\mathbf{u}}^n + (\nabla \cdot (\nu_E \nabla \bar{\mathbf{u}}^n) + \mathbf{F}^e)\Delta t \tag{9}$$

The auxiliary velocity field $\bar{\mathbf{u}}^*$ is usually not divergence free but this is imposed upon $\bar{\mathbf{u}}^{n+1}$. Hence, the auxiliary velocity is projected on the divergence-free space by writing the divergence of Eq. (8) as

$$\nabla \cdot \left(\frac{\bar{\mathbf{u}}^{n+1} - \bar{\mathbf{u}}^*}{\Delta t} \right) = -\nabla \cdot \left(\frac{1}{\rho} \nabla \bar{p}^{n+1} \right) \tag{10}$$

With the condition of incompressibility on $\bar{\mathbf{u}}^{n+1}$, this leads to the following pressure equation:

$$\nabla \cdot \left(\frac{1}{\rho} \nabla \bar{p}^{n+1} \right) = \frac{\nabla \cdot \bar{\mathbf{u}}^*}{\Delta t} \tag{11}$$

Since a constant density is considered here, Eq. (11) can be rewritten as

$$\nabla^2 \bar{p}^{n+1} = \frac{\rho}{\Delta t} \nabla \cdot \bar{\mathbf{u}}^* \tag{12}$$

where ∇^2 is the Laplacian operator.

Once pressure is obtained from Eq. (12), the velocity is updated by the computed pressure gradient:

$$\bar{\mathbf{u}}^{n+1} = \bar{\mathbf{u}}^* - \left(\frac{1}{\rho} \nabla \bar{p}^{n+1} \right) \Delta t \tag{13}$$

Finally, particles move only with this corrected velocity by the relation given by Eq. (5). One should note that the updated velocity $\bar{\mathbf{u}}^{n+1}$ is divergence free only within the spatial truncation error due to the method of solving Eq. (12) (see Section 3.2). It hence produces errors in particle positions, however, this error is still less than that of the WCSPH method [4].

3. SPH formulations

3.1. Core of SPH

In physical space, fluid can be discretised by a finite number of macroscopic volumes of fluid. In SPH, a particle a represents a macroscopic volume of fluid. Each fluid particle, for example particle a, carries information of a mass m_a, a density ρ_a, a pressure p_a, a velocity $\mathbf{u}_a$, a position $\mathbf{r}_a$ and other quantities depending on the nature of the flow and of the fluid. The mass is constant through the simulations, however, pressure, velocity, position and other physical quantities are updated every time step. Density is also updated every time step in WCSPH whereas constant density is set in ISPH.

A basic principle in SPH is that a quantity α can be expressed in terms of a convolution product of α and the Dirac distribution δ over the whole domain as

$$\alpha(\mathbf{r}) = \int_\Omega \alpha(\mathbf{r}')\delta(\mathbf{r} - \mathbf{r}')\, \mathrm{d}\mathbf{r}' \tag{14}$$

where Ω is the volume of the fluid domain, and $\mathrm{d}\mathbf{r}'$ an elementary volume. The Dirac distribution can be approximated in discrete sense by a kernel function w_h with smoothing length h, which allows any quantity to be expressed in terms of its values known at different particle locations [11,6,12]. More precisely, any quantity α attached to a particle "a" at a position $\mathbf{r}_a$ is written as

$$\alpha(\mathbf{r}_a) \approx \sum_b \frac{m_b}{\rho_b} \alpha_b w_h(r_{ab}) \tag{15}$$

where the subscript "b" is used to describe any particle in the neighbourhood of particle "a". The distance from "a" to "b" is $r_{ab}(=|\mathbf{r}_{ab}|)$, α_b denotes the value of any quantity α at $\mathbf{r}_b$ and the summation applies to all the particles, with the volume $\mathrm{d}\mathbf{r}'$ in Eq. (14) replaced by the particle volume $\frac{m_b}{\rho_b}$ in Eq. (15). According to Morris et al. [15], a kernel function w_h can be written in a general manner as

$$w_h(r_{ab}) = \frac{1}{h^\sigma} f\left(\frac{r_{ab}}{h} \right) \tag{16}$$

where σ is the dimension of the system and the smoothing length h is proportional to the particle distance, which plays a role similar to the mesh size in Eulerian codes. As shown in Eq. (16), the kernel only varies with the distance r_{ab} between particles, which ensures angular momentum conservation [13]. The kernel has to be at least C^1 for numerical consistency [13].

The gradient of α is then expressed as a function of α and the kernel derivatives as

$$\nabla \alpha(\mathbf{r}_a) \approx \sum_b \frac{m_b}{\rho_b} \alpha_b \nabla_a w_h(r_{ab}) \tag{17}$$

where the quantity $\nabla_a w_h(r_{ab})$ denotes the gradient of the kernel, which is taken as centered on the position of particle a.

Note that various ways exist to express gradients in continuous form, i.e.,

$$\nabla\alpha = \frac{1}{\rho}(\nabla(\rho\alpha) - \alpha\nabla\rho) \tag{18}$$

or

$$\nabla\alpha = \rho\left(\nabla\left(\frac{\alpha}{\rho}\right) + \frac{\alpha}{\rho^2}\nabla\rho\right) \tag{19}$$

which leads to different discrete SPH forms. For instance, combining Eqs. (17) and (18) gives the following SPH form:

$$\nabla\alpha(\mathbf{r}_a) \approx \frac{1}{\rho_a}\sum_b m_b(\alpha_b - \alpha_a)\nabla_a w_h(r_{ab}) \tag{20}$$

and with Eqs. (17) and (19):

$$\nabla\alpha(\mathbf{r}_a) \approx \rho_a\sum_b m_b\left(\frac{\alpha_a}{\rho_a^2} + \frac{\alpha_b}{\rho_b^2}\right)\nabla_a w_h(r_{ab}) \tag{21}$$

Here, Eq. (20) is symmetric and (21) is asymmetric when a and b are swapped. The second form ensures linear momentum conservation [13] and is used for pressure gradient.

However, since ρ is constant for each particle ($\rho_a = \rho_b$) for truly incompressible flow, Eqs. (20) and (21) are identical to Eq. (17). As a proof, since $\rho_a = \rho_b = \rho_0$, the right hand side of Eq. (21) can be split in two parts:

$$\rho_b\sum_b m_b\frac{\alpha_a}{\rho_b^2}\nabla_a w_h(r_{ab}) + \rho_b\sum_b m_b\frac{\alpha_b}{\rho_b^2}\nabla_a w_h(r_{ab}) \tag{22}$$

Then it reduces to

$$\alpha_a\sum_b\frac{m_b}{\rho_b}\nabla_a w_h(r_{ab}) + \sum_b\frac{m_b}{\rho_b}\alpha_b\nabla_a w_h(r_{ab}) \tag{23}$$

If the kernel is built in such a way that for a constant field α, $\nabla\alpha = 0$ holds, then one has

$$\sum_b\frac{m_b}{\rho_b}\nabla_a w_h(r_{ab}) = 0 \tag{24}$$

The first term of Eq. (23) then vanishes, which leads to the SPH formalism as Eq. (17). However, in the following, the kernel used here does not satisfy exactly the condition given by Eq. (24), thus Eq. (20) or Eq. (21) is kept to estimate gradients. What holds for gradient also holds for divergence. One example of each operator follows: the gradient of pressure can be expressed as

$$\nabla\bar{p}_a \approx \rho_a\sum_b m_b\left(\frac{\bar{p}_b}{\rho_b^2} + \frac{\bar{p}_a}{\rho_a^2}\right)\nabla_a w_h(r_{ab}) \tag{25}$$

and the divergence of velocity is

$$\nabla\cdot\bar{\mathbf{u}}_a \approx -\frac{1}{\rho_a}\sum_b m_b\bar{\mathbf{u}}_{ab}\cdot\nabla_a w_h(r_{ab}) \tag{26}$$

with $\bar{\mathbf{u}}_{ab} = \bar{\mathbf{u}}_a - \bar{\mathbf{u}}_b$. Note that other forms of gradient or divergence exist. Some of them are presented in [13].

The viscous term is not directly built as divergence of gradient, but as a combination of the finite difference approach and SPH formalism. For instance, the viscous term by Cleary and Monaghan [3] reads

$$\nabla\cdot(\nu_E\nabla\bar{\mathbf{u}}_a) \approx \sum_b m_b\left(8\frac{\nu_{E,a} + \nu_{E,b}}{\rho_a + \rho_b}\frac{\bar{\mathbf{u}}_{ab}\cdot\mathbf{r}_{ab}}{r_{ab}^2 + \eta^2}\right)\nabla_a w_h(r_{ab}) \tag{27}$$

and by Morris [15] is

$$\nabla\cdot(\nu_E\nabla\bar{\mathbf{u}})_a \approx \sum_b m_b\left(\frac{\rho_a\nu_{E,a} + \rho_b\nu_{E,b}}{\rho_a\rho_b}\frac{\mathbf{r}_{ab}\cdot\nabla_a w_h(r_{ab})}{r_{ab}^2 + \eta^2}\right)\bar{\mathbf{u}}_{ab} \tag{28}$$

where $\nu_{E,a} = \nu_a + \nu_{T,a}$ and $\eta^2 = 0.01h^2$ is a parameter to avoid a zero denominator. As pointed out by Morris et al., this term performs better for laminar flows [15]. However, Monaghan's term is retained for the simulations presented in the following since the results from both methods show little difference [7]. For turbulent flows, the turbulent viscosity $\nu_{T,a}$ is estimated through turbulence closures such as mixing length (l_m), one equation ($k - l_m$) or two equations (k–ϵ) models. The detail of these turbulence closures as implemented in the SPARTACUS-2D code are presented in [22].

The time step Δt is chosen by the same expression for WCSPH and ISPH, i.e., the minimum of three conditions, the CFL condition, and the mass and viscous force conditions such that

$$\Delta t = \min\left(0.4\frac{h}{|\bar{u}_{\mathrm{ref}}|}, 0.25\ \min_a \sqrt{\frac{h}{|\mathbf{f}_a|}}, 0.125\ \min_a \frac{h^2}{\nu_{\mathrm{E},a}}\right) \tag{29}$$

where $\mathbf{f}_a$ is the force per unit mass, equivalent to the magnitude of particle acceleration, and $|\bar{u}_{\mathrm{ref}}|$ is the reference velocity, which will be respectively the numerical speed of sound c_0 and maximum fluid velocity $|\bar{u}_{\max}|$ for WCSPH and ISPH.

3.2. Pressure Poisson equation

Cummins et al. [4] described two approaches to solve the pressure equation, the first by an exact discretisation of the Laplacian and the second by an approximation to it. They observed that using an exact Laplacian formulation shows a checker-board effect similar to the one observed in an Eulerian approach with a collocated arrangement of the pressure and velocity. To circumvent this problem, an approximate Laplacian operator with the same form as a diffusion term (i.e., analogous to Eq. (28), see [23] for coding details) is used and reads

$$\nabla^2 \bar{p}_a \approx \frac{2}{\rho_a} \sum_b m_b \frac{\bar{p}_{ab}\mathbf{r}_{ab} \cdot \nabla_a w_h(r_{ab})}{r_{ab}^2 + \eta^2} \tag{30}$$

where $\bar{p}_{ab} = \bar{p}_a - \bar{p}_b$.

The linear system is solved by the Bi-CGSTAB method [25] without pre-conditioning.

The residual $(R)_a$ is defined as $(R)_a = (B)_a - (Lp)_a$, where $(B)_a = (\rho\nabla \cdot \bar{\mathbf{u}}^*/\Delta t)_a$ and $(Lp)_a = (\nabla^2 \bar{p})_a$. The convergence is obtained when

$$\frac{\|R\|_2}{\|R_0\|_2} < 10^{-2} \tag{31}$$

where R_0 is the initial residual and $\|\cdot\|_2$ the l_2-norm calculated as

$$\|R\|_2 = \sqrt{\sum_{a=1}^{N} R_a^2} \tag{32}$$

where N is the number of particles. The convergence criterion can be further adjusted to suit the applications.

3.3. Boundary conditions

Flows of interest in this paper are either periodic in the streamwise direction, or have a free-surface, or are wall-bounded. Periodic boundary conditions are straightforward, the particles going out of the domain through one side being re-injected through the opposite side. For free-surface treatment, zero pressure needs to be applied in ISPH while the pressure is obtained by the knowledge of density [14] in WCSPH. Surface particle tracking, which is a key point in ISPH for free-surface flow, is investigated in Section 3.3.2. At a wall, Dirichlet boundary conditions apply to velocity and Neumann conditions should be applied to pressure in both methods (see [24] in terms of WCSPH). Difficulties in ISPH arise when pressure wall boundary conditions need to be set together with Dirichlet boundary conditions on the velocity.

3.3.1. The use of dummy particles

Unlike finite differences where skewed discretisations can be introduced near a wall to retain the same order (high order backward differencing), SPH has a large isotropic stencil which becomes truncated near a wall. With a crude discretisation we observe that particles can penetrate and even cross the walls. There are several ways to prevent this phenomenon, for example, by using mirror particles [4] or some repulsive forces [14], or dummy particles [19]. Mirror particles are set either symmetrically or asymmetrically to fluid particle positions and have a non-zero velocity. On corners or curved surfaces these particles no longer have homogeneous distribution of spacing which leads to large density variations. With repulsive forces, only one layer of particles is placed on the wall, and as indicated by the name, they exert very large repulsive forces to prevent fluid particles from crossing the walls. The order of the scheme is then degraded and particles tend to "wobble" when moving parallel to the wall. Among these techniques, dummy particles are used here. They are regularly distributed at the initial state and have zero velocity through the whole simulation, while several layers of dummy particles [19] are built as an extension of the edge particles surrounding the solid boundaries to ensure the same order of discretisation (in terms of kernel compact support) for particles located close to those boundaries, as for particles located in the core of the domain. This also makes the coding simpler (e.g., for parallelisation) as the same scheme is used for all particles with the only difference that wall particles are not displaced at the end of the time step. The number of dummy particle layers is decided from the radius of the compact support (i.e., such that the stencil is not truncated for the near-wall particles). In the following simulations, four layers of dummy particles are built. Dummy particles do not move but carry an identical pressure to edge

particles normal to the wall (see Fig. 1). To illustrate the use of dummy particles, two types of wall configurations are shown: the first where the dummy particles are in the outer corner (see Fig. 1(a)) and the second for the inner corner (Fig. 1(b)). There is no special treatment when outer corners are considered in contrast to what happens at inner corners where two pressure fields overlap with the presence of the two perpendicular walls. To circumvent this problem in this work, the diagonal particles carry the same information as the average of their four neighbouring particles. The influence of the dummy particles on the solution is examined in the following subsection.

3.3.2. Surface particle tracking

No dummy particles are used to set the free-surface boundary conditions. For that reason, the number of neighbouring particles are smaller than what it should be since the support of the kernel is truncated (see Fig. 2). This property is used to define the free surface and to impose zero pressure on the surface particles. Divergence of a particle position in SPH reads

$$\nabla \cdot \mathbf{r} = \sum_b \frac{m_b}{\rho_b} \mathbf{r}_{ab} \cdot \nabla_a w_h(r_{ab}) \tag{33}$$

This is equal to 2 for 2-D simulations in the core of the domain and much below 2 for surface particles. Hence, a criterion set to 1.5 is used to determine which particles belong to the surface (see Eq. (33)). The dam-breaking case (see Section 6 for a more complete description) is used to illustrate the method. The identified surface particles are shown in Fig. 3 at different times. Most surface particles at the surface are identified but not all of them, this defect is acceptable, as the undetected surface particles still have a pressure very close to zero. However, this could be further improved.

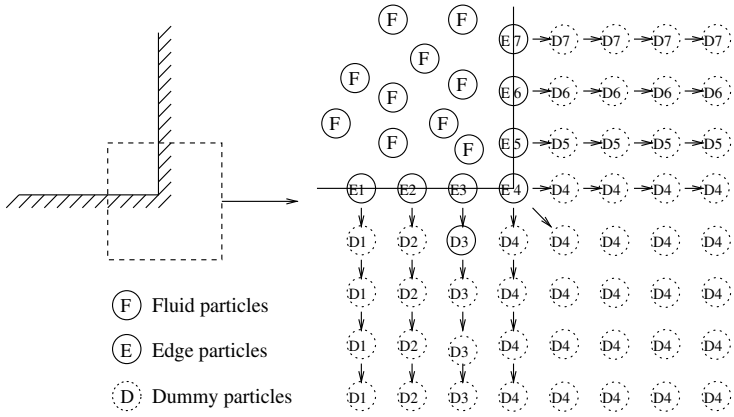

(a) Outside (identical number=identical pressure)

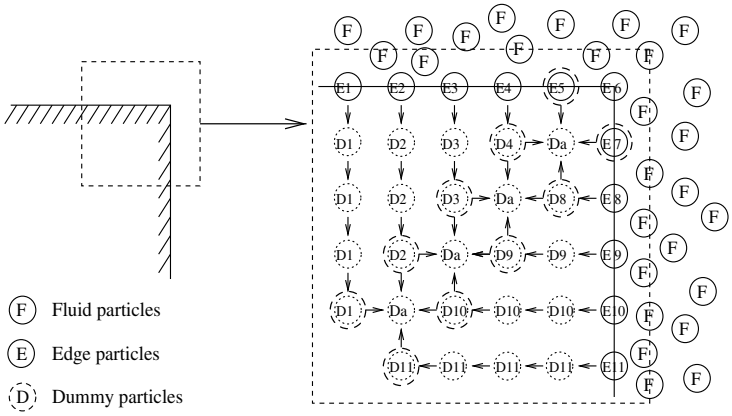

(b) Inside (D_a=the average of 4 neighbouring particles)

Fig. 1. Sketch of dummy particles around a wall corner: (a) case of an outer corner (example of a cavity flow) and (b) case of an inner corner (example of a square cylinder in a flow).

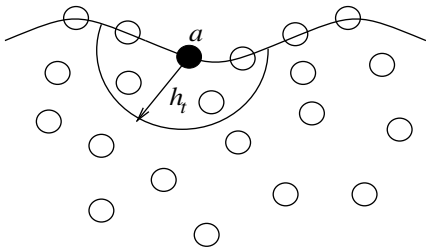

Fig. 2. Zoom of a free surface. Description of the kernel compact support for a surface particle.

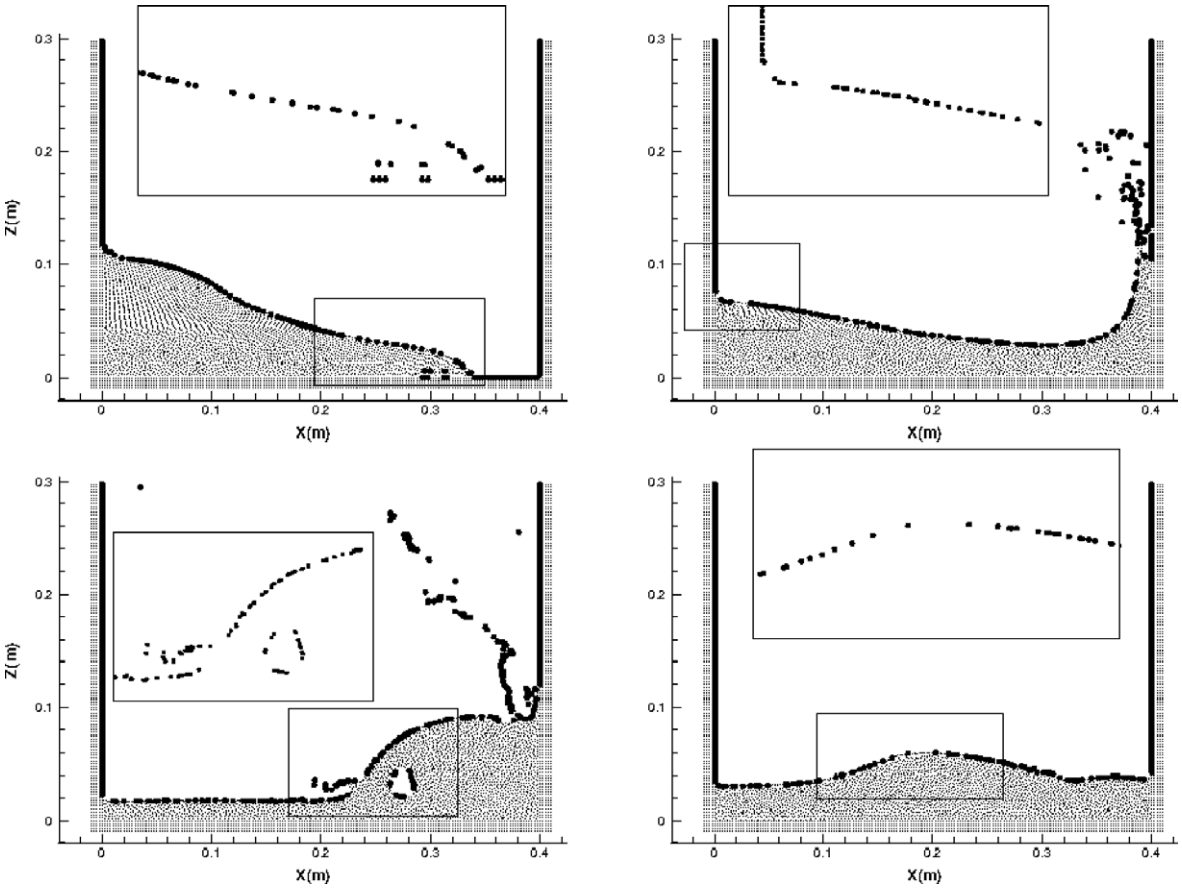

Fig. 3. Examples of surface particle tracking defect (dam-breaking case, top left: $t = 0.186$ s, top right: $t = 0.278$ s, bottom left: $t = 0.650$ s, bottom right: $t = 1.860$ s).

4. Lid-driven cavity flow

The lid-driven cavity flow has been widely used as a benchmarking test case for various numerical methods in the last decades and is thus suitable for testing the WCSPH and ISPH algorithms. Two different Reynolds numbers, based on the lid velocity and the size of the cavity, namely 400 and 1000, are studied and results are compared to Ghia et al. data [5] and to a finite volume based software (STAR-CD) data. The last data is referred to as FV.

4.1. Simulation conditions

This case is purely numerical and the cavity size L, the lid velocity U_{Lid} and the density ρ are set to unity, such that $\nu = \frac{1}{Re}$. The lid wall and solid walls consist of a layer of edge particles and four layers of dummy particles. The lid moves at a constant velocity. The configuration of the geometry is shown in Fig. 4. Three different initial fluid particle distributions are presented for WCSPH and ISPH at $Re = 400$, with initial distances dr between closest neighbouring particles of $L/40$, $L/70$ and $L/100$. At

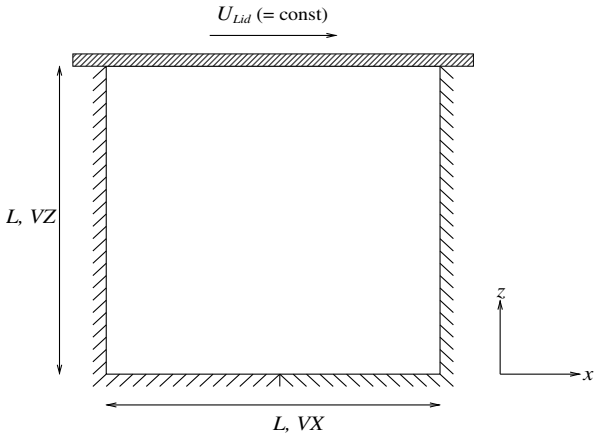

Fig. 4. 2-D lid-driven cavity flow configuration. Geometry (L is the cavity size, VX horizontal velocity, VZ vertical velocity) and lid velocity (U_{Lid}).

Re = 1000, seven different initial fluid particle distributions are presented for both WCSPH and ISPH, starting from the coarsest one with dr = L/20. The other distributions are respectively based on dr = L/40, dr = L/80, dr = L/120, dr = L/160, dr = L/200, and finally dr = L/240.

In terms of SPH parameters, a fourth order of kernel [15] with a smoothing length ratio h/dr of 1.3 is used in both WCSPH and ISPH. The numerical speed of sound in WCSPH is set at $c_0 = 100\,U_{\mathrm{Lid}}$ instead of the normal definition of speed of sound $c_0 = 10U_{\mathrm{Lid}}$ in order to cure the appearance of a void at the center of the cavity; this phenomenon having already been reported in [8]. In the following simulations, dummy particles are involved in the Laplacian operator. The right hand side of Eq. (12) for edge particles is the same as for fluid particles instead of zero.

FV simulations are performed on a grid identical to that Ghia et al. [5] used with 128 cells in horizontal and vertical directions (dr = L/128). The spatial discretisation is second-order accurate, the velocity coupling is achieved by the SIMPLE algorithm, and the steady state is reached for a non-dimensional tolerance of 10^{-10} (see Eq. (31)).

4.2. Results

At first, WCSPH and ISPH are run at Re = 400 to examine the influence of spatial resolution and results are plotted in Fig. 5 along with FV data, which correspond to Ghia et al. [5]. Horizontal and vertical velocity component profiles from WCSPH for dr = L/40 look unrealistic. Higher resolutions produce more realistic results but still far from FV data (see Fig. 5(a) and (c)). On the other hand, ISPH gives a good estimation of both horizontal and vertical velocity components, even with the lowest resolution (dr = L/40) (see Fig. 5(b) and (d)).

Next, the Reynolds number is increased to 1000 and the initial particle distance dr between the closest neighbouring particles is L/20, L/40, L/80, L/120, L/160, L/200 and L/240. Horizontal and vertical velocity components depending on the initial particle distributions are plotted in Fig. 6 against Ghia et al. and FV data (dr = L/128).

Again, WCSPH shows significant influence of the resolution or initial particle distribution, with results for the coarser cases dr = L/20 and L/40 being very far from the FV profiles (see Fig. 6(a) and (c)). With WCSPH, the wall boundary layers are significantly thicker and this leads to severely underestimated velocity profile extremes. It is as if the viscosity was being strongly increased for coarser resolutions. This may be attributed to the random motion of particles ("wobble" due to large pressure fluctuations) which enhances momentum diffusion in a Brownian-like fashion. Animations show that this "wobble" is much smaller with ISPH than WCSPH. Moreover with WCSPH, the central solid body rotation effect does not seem to be captured properly (see Fig. 6(a)). Indeed, profiles at dr = L/160, dr = L/200, dr = L/240 fall almost on top of each other, which may indicate that there is an asymptotic convergence, but not towards the FV solution, as proved by the difference in the position of the minimum of the horizontal velocity component for WCSPH and FV. On the other hand, ISPH shows a much smoother pattern (see Fig. 6(b) and (d)) with regular but perhaps slow asymptotic convergence towards the accurate results of Ghia et al. [5]. The l_1-norm applied to the vertical and horizontal velocity components is used to perform the error analysis, rather than the classical l_2-norm. As no analytical solution is available for this case, the data obtained by a very fine FV simulation (dr = L/1024) are used as a reference. The l_1-norms of the error on both velocity components are plotted against particle spacing dr in Fig. 7 for WCSPH, ISPH and FV. Spatial order of accuracy can be estimated as of the order of unity for both WCSPH and ISPH, and it is of second order for FV, as expected. While the symmetrical formulation of SPH may lead one to expect second-order accuracy, this is clearly not the case for several reasons. This flow is dominated by viscous forces and boundary conditions. The latter can seriously decrease the order and the discretisation of the Laplacian operator, whether by Eq. (27) or (28), is rather crude. Further effects that reduce the order are for instance the irregular distribution of the particles (as opposed to the initial square lattice distribution [1]) and the ratio of smoothing length to particle spacing, see [18] for instance. A full analysis of these issues is beyond the scope of this paper. Pressure profiles are plotted in Fig. 8; comparisons

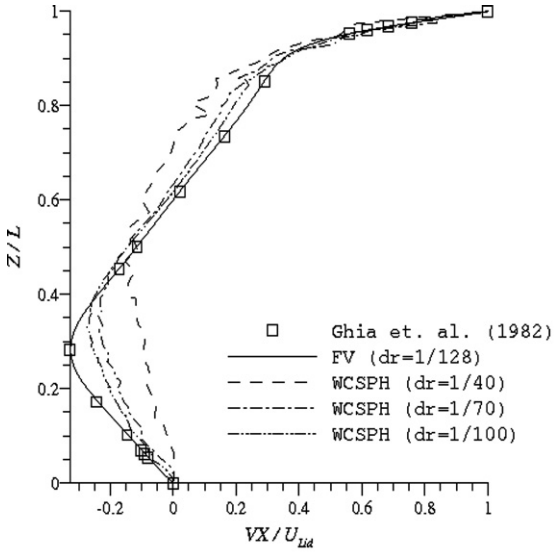

(a) Axial velocity profiles in $X = L/2$ (WCSPH).

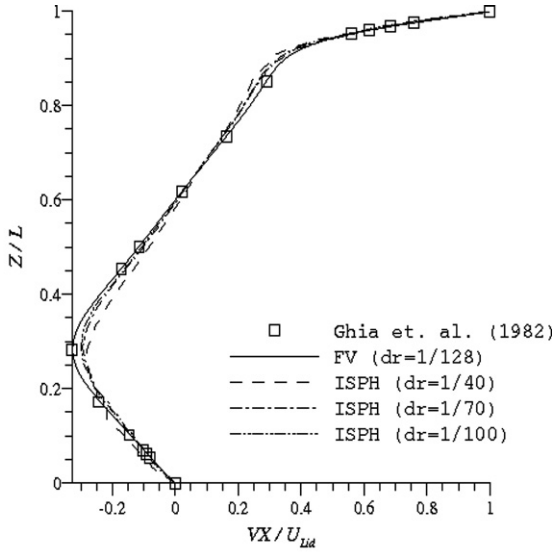

(b) Axial velocity profiles in $X = L/2$ (ISPH).

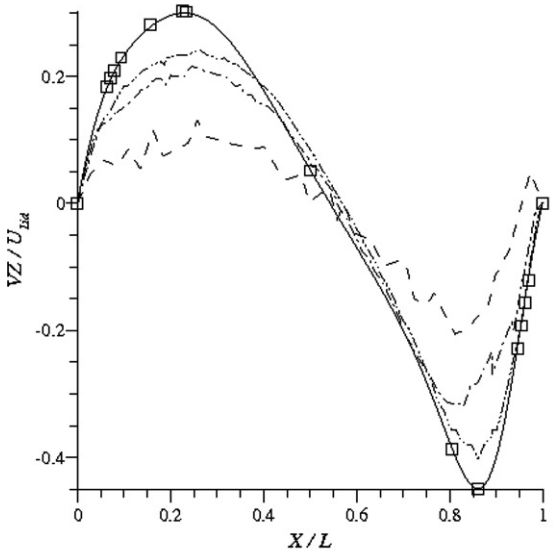

(c) Vertial velocity profiles in $Z = L/2$ (WCSPH).

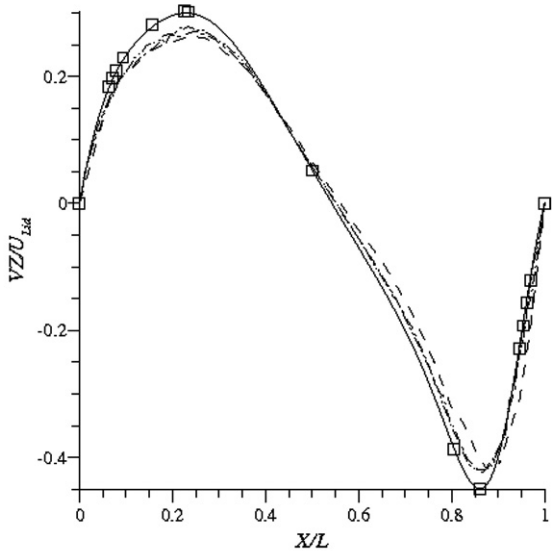

(d) Vertial velocity profiles in $Z = L/2$ (ISPH).

Fig. 5. 2-D SPH lid-driven cavity flow velocity profiles at t = 52.0 against Ghia et al. [5] and converged FV data for Re = 400. Spatial resolution influence.

of axial variation of pressure for both SPH methods with FV are shown in Fig. 8(a) and of diagonal variation of pressure for ISPH with FV in Fig. 8(b). The pressure field is very noisy for WCSPH in contrast to the ISPH pressure field, which is very smooth. Moreover, ISPH isobars show a trend very close to FV. Velocity vectors are now compared. WCSPH and ISPH simulations both capture the secondary flows observed at this Reynolds number in the left and right bottom corners of the cavity. Fig. 9 (left) gives a zoom of the left top corner for WCSPH (Fig. 9(a)), ISPH (Fig. 9(c)) and FV (Fig. 9(e)). However, the velocity in the first layer of fluid particles is very non-smooth when predicted by WCSPH. Fig. 9 (right) gives a zoom of the right bottom corner vortex for WCSPH (Fig. 9(b)), ISPH (Fig. 9(d)) and FV (Fig. 9(f)), where unit vectors are used to show direction. The center of the right secondary vortex is well predicted by all methods: WCSPH (0.85; 0.10), ISPH (0.87; 0.11) and FV (0.86; 0.11). Once again, the WCSPH wall treatment is not smooth. Overall, ISPH shows more coherent velocity fields while WCSPH exhibits small scale instabilities mentioned earlier.

The time step and CPU time for the case of Re = 1000 are indicated in Table 1. The simulations were carried out on a Intel (R) PENTIUM D CPU 3.2 GHz with 2.0 G RAM with 32 bits.

The longer CPU time in WCSPH can be explained by the fact that high numerical speed of sound required to prevent the appearance of a void in the cavity center requires the use of a very small time step. Such voids had also appeared in the

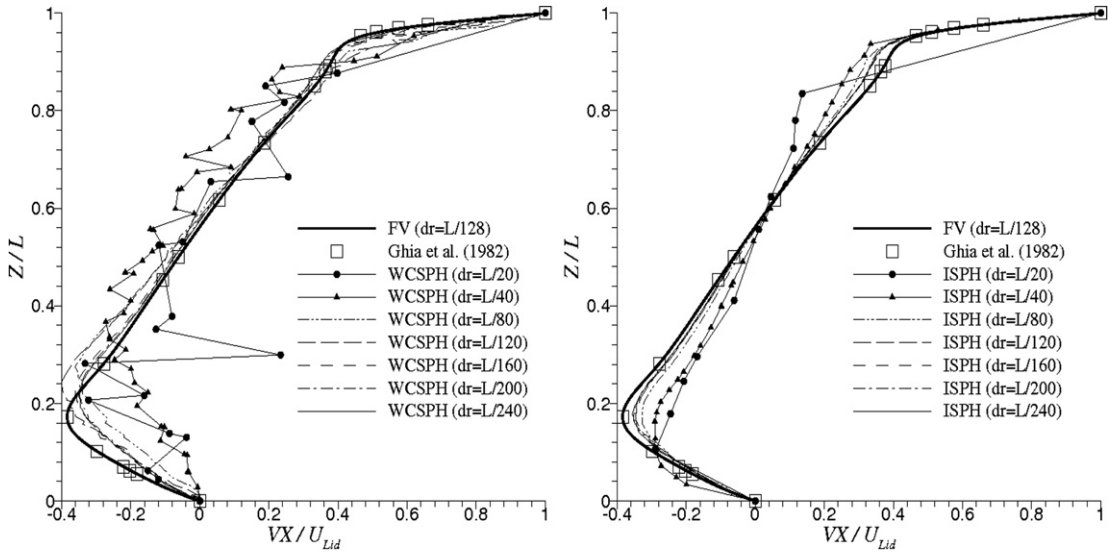

(a) Axial velocity profiles in $X = L/2$ (WCSPH). (b) Axial velocity profiles in $X = L/2$ (ISPH).

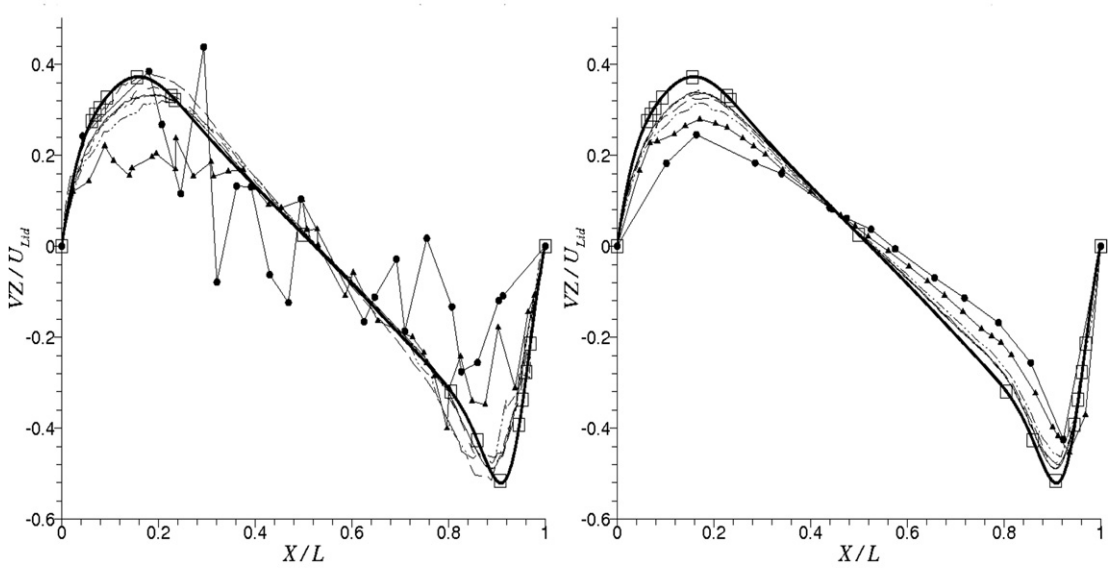

(c) Vertial velocity profiles in $Z = L/2$ (WCSPH). (d) Vertial velocity profiles in $Z = L/2$ (ISPH).

Fig. 6. 2-D SPH lid-driven cavity flow velocity profiles at $t = 52.0$ against Ghia et al. [5] and converged FV data for $Re = 1000$. Spatial resolution influence.

recirculation behind hills or in the recirculation past a square cylinder presented below, inducing the use of a Mach number (Ma) of 0.01 in most applications rather than $Ma = 0.1$ as mentioned in [8].

5. Bluff body

Separated flows often take place in engineering problems as seen, for example, in flows over steps and fences, and around bluff bodies [16]. This is therefore a fundamental test case. Laminar simulations around a bluff body are attempted here at two different Reynolds numbers ($Re_d = 20$ and 100), based on the bulk velocity and the size of the square cylinder. WCSPH and ISPH are again compared with FV (STAR-CD).

5.1. Simulation conditions

The geometry of the configuration is based on Kim et al. [10] and shown in Fig. 10. All parameters are normalised here like in the lid-driven cavity flow case. The square cylinder edge size d, the mean bulk velocity at the inlet U_0 and the density ρ are

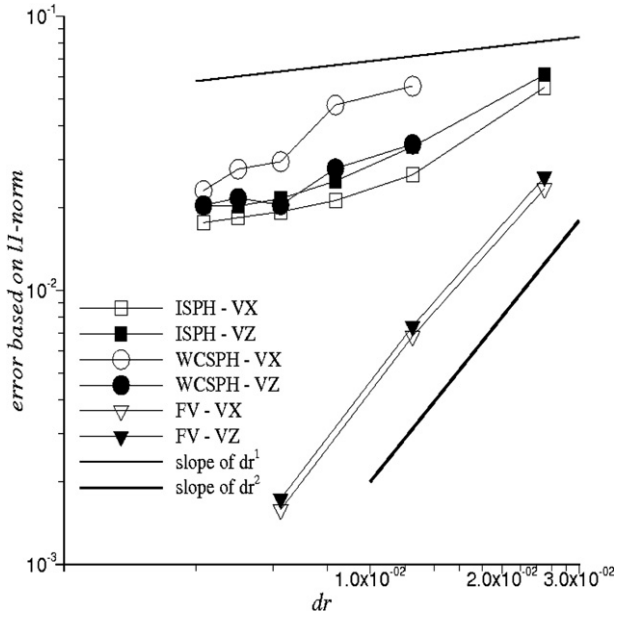

Fig. 7. Lid-driven cavity flow error estimation versus spatial resolution influences for WCSPH, ISPH and FV for $Re = 1000$.

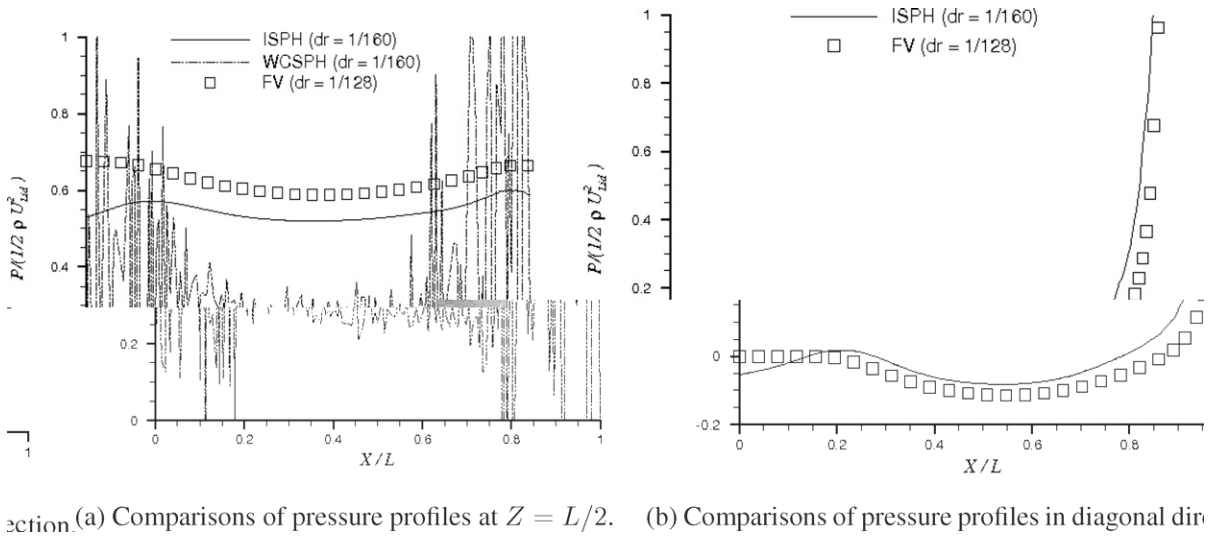

ection (a) Comparisons of pressure profiles at $Z = L/2$. (b) Comparisons of pressure profiles in diagonal dir

Fig. 8. 2-D SPH lid-driven cavity flow pressure profiles at $t = 52.0$ against to converged FV for $Re = 1000$. (a) Axial variation of pressure profile at $Z = L/2$, WCSPH (d$r = L/160$), ISPH (d$r = L/160$) and FV (d$r = L/128$). (b) Diagonal variation of pressure profiles between ISPH and FV.

set to unity. The Reynolds number based on the mean bulk velocity and the width of the cylinder is small enough to ensure laminar flow ($Re_d = 20$ and 100). The cylinder is located centrally in between two flat plates a distance of $5d$ apart; the upstream end of the domain is $3d$ from the cylinder and the length to the downstream end $L_d = 28d$ for $Re_d = 20$ and $L_d = 98d$ for $Re_d = 100$, to ensure that the flow re-develops downstream of the cylinder. Periodic inflow–outflow boundary conditions are imposed, the flow being driven by a force relative to the prescribed mean bulk velocity at the inlet, which allows constant flow rate. In total, 69,748 particles are used (63,018 fluid particles, 1362 edge particles and 5368 dummy particles) for both WCSPH and ISPH at $Re_d = 20$. Initially, the particles are regularly distributed with a distance dr = d/20. For $Re_d = 100$, the total of 222,348 particles are used (201,618 fluid particles, 4162 edge particles and 16,568 dummy particles) for both WCSPH and ISPH with the initial particle distribution dr = d/20. In terms of SPH parameters, the same fourth order of kernel as for cavity tests, associated to a smoothing length ratio h/dr of 1.3, is used. Running WCSPH with the usual numerical speed of sound value leads to the appearance of a void downstream of the cylinder, this phenomenon having also been observed for the lid-driven cavity case (see Section 4). In ISPH in contrast, this void does not occur. The numerical speed of sound is set at

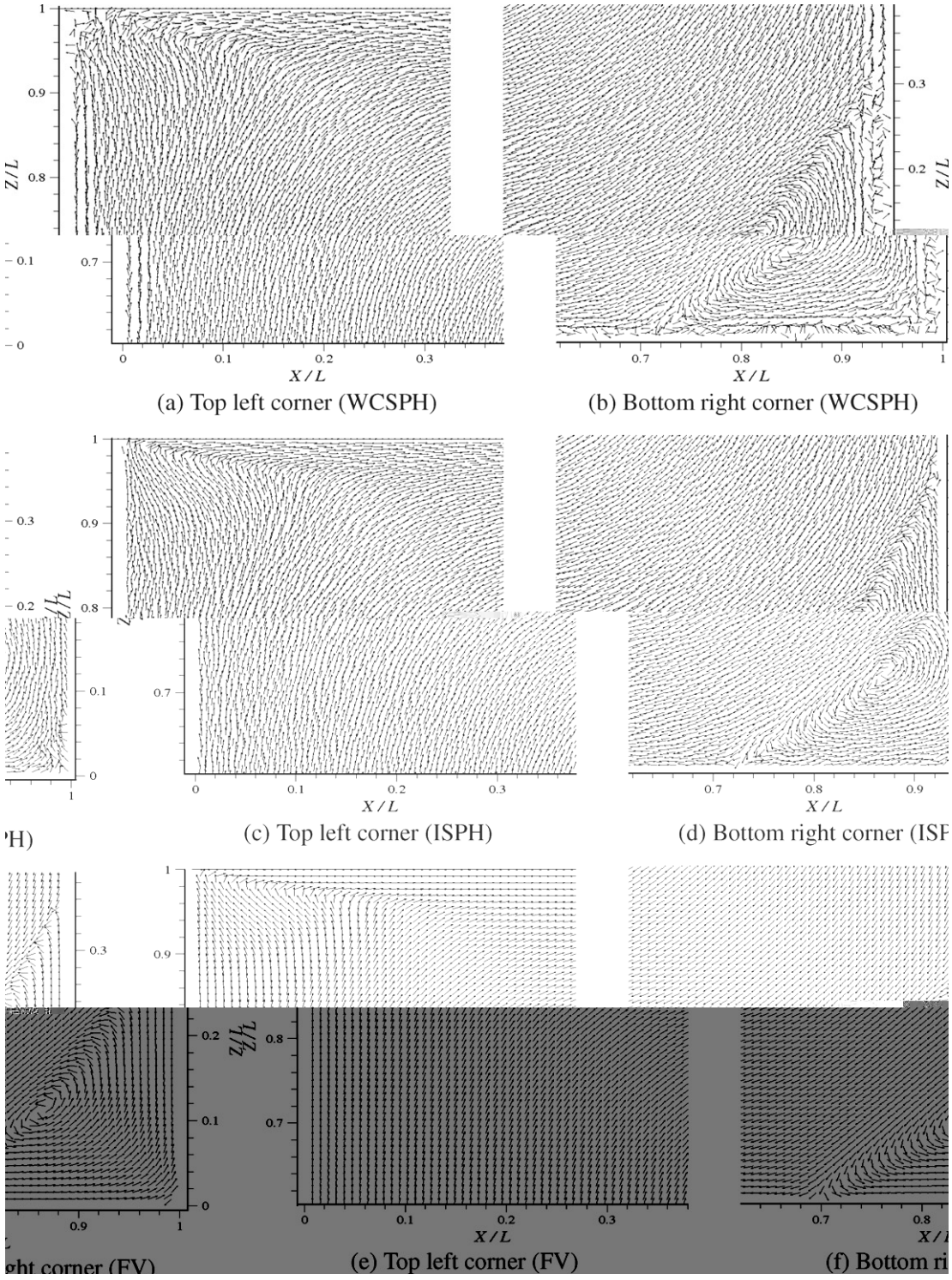

Fig. 9. 2-D SPH lid-driven cavity flow uniform velocity magnitude at $t = 52.0$ against to converged FV for $Re = 1000$. (a,b) WCSPH (d$r = L/160$, non-smooth pattern) (d$r = L/128$); (c,d) ISPH (d$r = L/160$, smooth pattern); (e,f) FV. (a,c,e) Velocity vectors at the top left corner of the cavity. (b,d,f) Secondary flow at the bottom right corner.

$c_0 = 100U_0$ for WCSPH. No experimental data or analytical formulae are available for this case to our knowledge. SPH results here are thus compared to data obtained by FV (STAR-CD) with a very fine uniform mesh spacing equal to dr = d/80. The first case at $Re_d = 20$ is run in steady motion with a central difference scheme for convection. The mesh has 1,017,600 cells. The

Table 1
Comparisons of the 2-D lid-driven cavity flow CPU time for $Re = 1000$ with $dr = L/160$ for all methods, up to time $t = 52.0$ for the SPH cases

Methods	ISPH	WCSPH	FV
Time step: dt	0.325×10^{-2}	0.325×10^{-4}	Steady
CPU time (h)	19.5	179	0.4

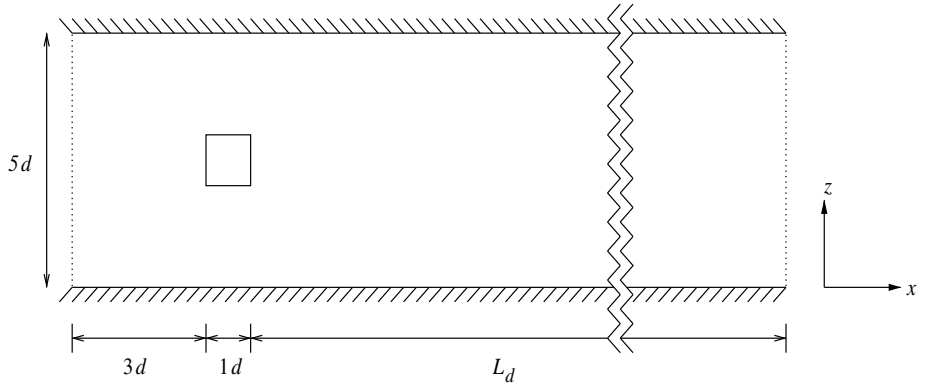

Fig. 10. Geometry of the 2-D bluff body.

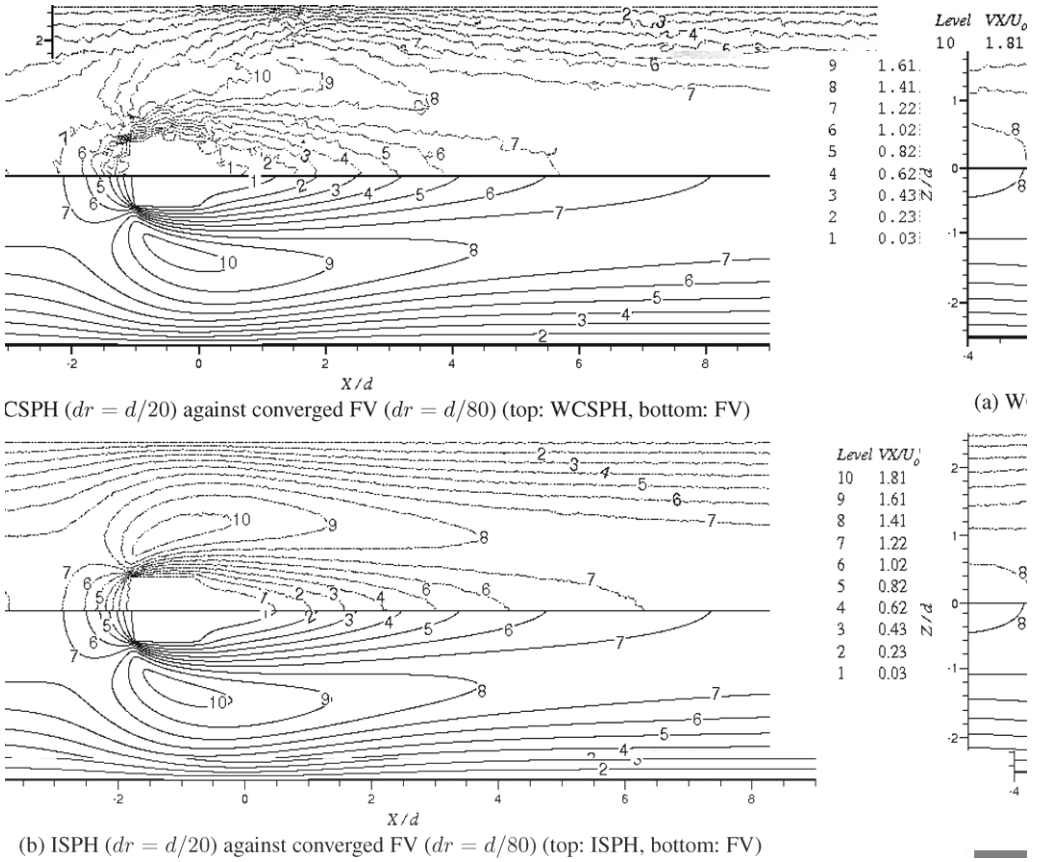

Fig. 11. Comparisons of horizontal velocity magnitude contours at $t = 322.0$ with for SPH ($dr = d/20$) and FV ($dr = d/80$) for $Re_d = 20$. A zoom from $X/d = -4$ to $X/d = 10$ is presented. (a) WCSPH results against FV contours. (b) ISPH results against FV contours (WCSPH and ISPH in dashed lines and FV in solid lines).

second Reynolds number of 100 is treated as a transient flow, with PISO to solve the velocity-coupling and an Euler implicit time stepping scheme. This combination (PISO and Euler) has been proven to be second-order accurate in time [17]. A central difference scheme is used for convection. The time step is then 0.0025 and the mesh has 3,193,600 cells.

5.2. Results

First of all, the results for $Re_d = 20$ are plotted in Fig. 11 for the dimensionless horizontal velocity magnitude contour. Both SPH results at the physical time of $t = 322.0$ are compared to the converged FV results. Solid lines correspond to FV results and dashed lines to both SPH methods (WCSPH against FV in Fig. 11(a) and ISPH against FV in Fig. 11(b)). The trend observed for the cavity flow also holds here, i.e., ISPH shows a smoother velocity field than WCSPH. Agreement of ISPH with FV is clearly quite close while WCSPH is less good. The pressure contour and profile at the center of the channel along the axial direction are respectively depicted in Figs. 12 and 13. WCSPH shows again scattered results (see the highly distorted isobar patterns for WCSPH in Fig. 12(a)) while ISPH shows smoother ones. The time-averaged pressure drag coefficient is calculated for the SPH method and steady state pressure drag coefficient for FV. WCSPH gives 14.56, ISPH 3.48 and FV 5.53. The origin of the difference has not been resolved and requires further investigation.

The Reynolds number of $Re_d = 100$ is high enough for the flow to shed, but small enough to keep it 2-D and laminar. The frequency f of the vortex shedding of WCSPH and ISPH is compared to FV's one. The Strouhal number $St = fd/U_0$ is calculated. WCSPH, ISPH and FV, respectively, give a period of $T_{WCSPH} = 5.20$, of $T_{ISPH} = 4.40$ and of $T_{FV} = 4.00$, and $St_{WCSPH} = 0.19$, $St_{ISPH} = 0.23$ and $St_{FV} = 0.25$. The dimensionless horizontal velocity magnitude contour is plotted for each method (see Fig. 14) when the flow is fully developed in all simulations. Four instants are considered, $0.25T$, $0.50T$, $0.75T$ and $1.00T$, where T is the period of the shedding for each method, i.e., $T = T_{WCSPH}$ for WCSPH, $T = T_{ISPH}$ for ISPH, $T = T_{FV}$ for FV. Both SPH methods show the shedding, but WCSPH one is not as pronounced as it should be, compared to FV. Former tests with $dr = d/10$ showed a void downstream of the cylinder, which is smaller with $dr = d/20$. On the other hand, ISPH shows a behaviour similar to FV's, the shedding looking good. The pressure time-averaged drag coefficient calculated for WCSPH, ISPH and FV are respec-

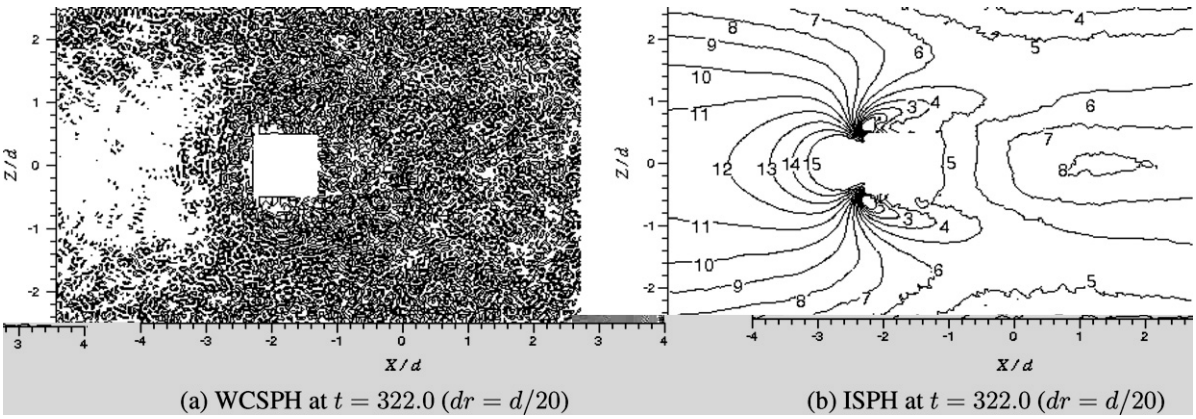

Fig. 12. Comparisons of instantaneous pressure contours around the square cylinder at the physical time $t = 322.0$ for SPH for $Re_d = 20$.

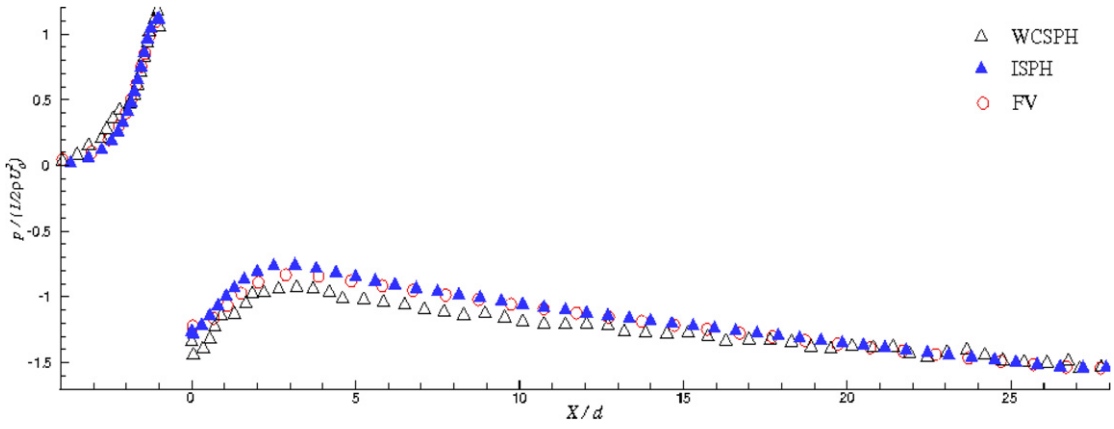

Fig. 13. Comparisons of time-averaged centerline pressure distributions from WCSPH (△), ISPH (▲) and FV methods (○) for $Re_d = 20$.

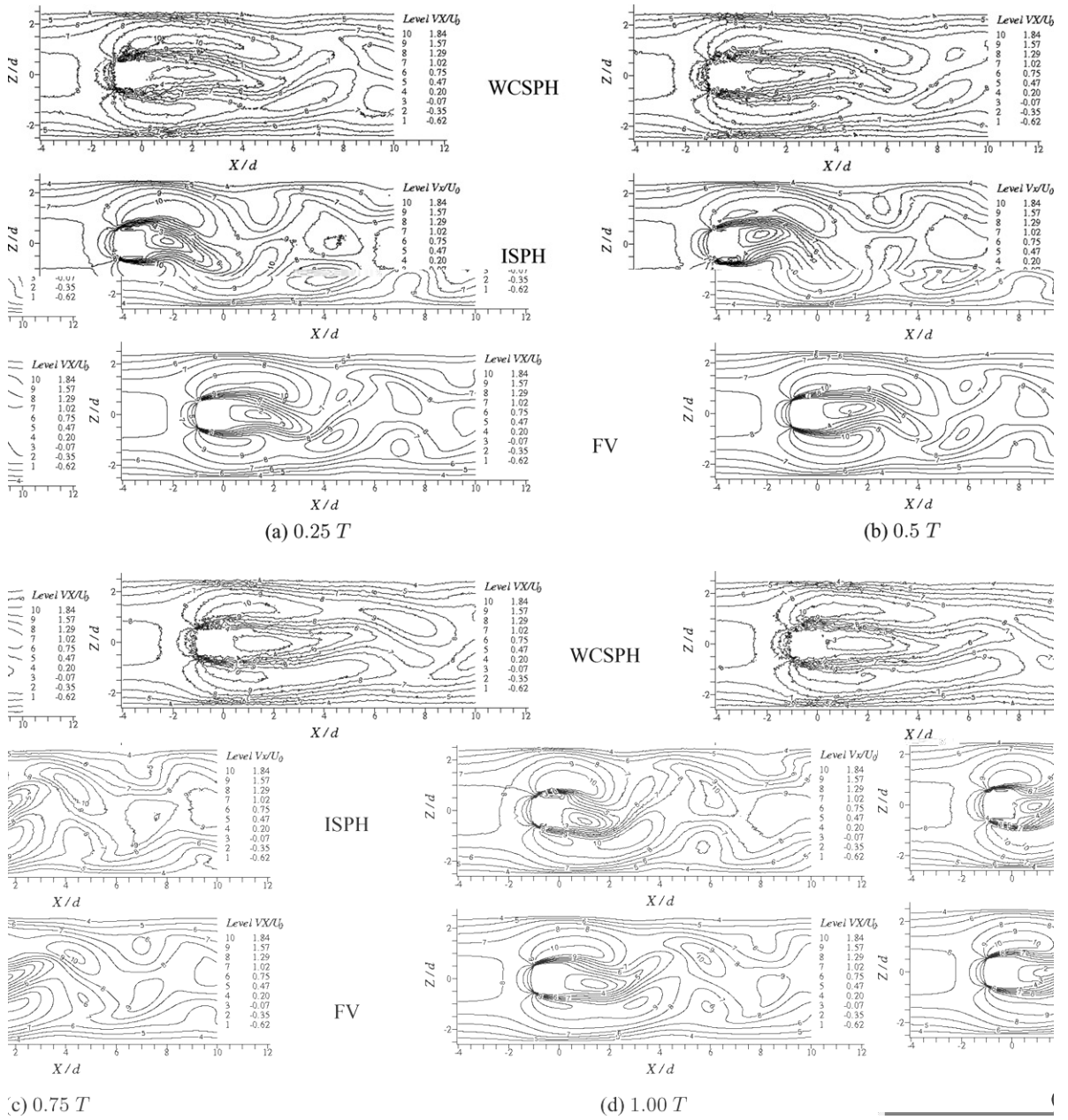

Fig. 14. Comparisons of WCSPH, ISPH and FV horizontal velocity contours at 4 various instants depending on their own shedding period: (a) 0.25T, (b) 0.5T, (c) 0.75T and (d) 1.00T, where $T = T_{WCSPH}$ for WCSPH, $T = T_{ISPH}$ for ISPH and $T = T_{FV}$ for FV.

tively 1.09, 6.30 and 3.23 and the lift coefficients are of −0.19, −0.04 and of 0.00, respectively. A possible explanation for the erroneous value of the drag and lift for WCSPH is the strong scattering in the pressure due to its calculation by the equation of state, which makes difficult the prediction of quantities deriving from the pressure. The CPU time for all methods is given in Table 2 with same spatial discretisation dr = 1/10 for SPH and FV. The small CPU time for ISPH is due to the small number of iterations needed for convergence of the pressure Poisson equation in this case.

6. Dam breaking

Dam-break flows are an important practical problem in civil engineering and have long been the subject of the analytical and experimental study [20]. In terms of numerical study, it highlights free surface and impact against wall boundary conditions.

Table 2
CPU time for the bluff body flow at $Re_d = 100$ with $dr = 1/10$ at the same physical time $t = 520.0$

Methods	ISPH ($dr = d/10$)	WCSPH ($dr = d/10$)	FV ($dr = d/10$)
Time step: dt	0.26×10^{-1}	0.52×10^{-3}	0.5×10^{-1}
CPU time (h)	13.0	305.5	42.9

Two sets of simulations are presented here, the first deals with a dry bed and the second is with a wet bed. The wet bed case is based on an experimental configuration [9]. As mentioned in Section 3, several choices for turbulence closures in the code are available. In this section, all the simulations are based on the k–ϵ model [7] and comparisons are made between WCSPH and ISPH.

6.1. Simulation conditions on dry bed

The geometry of a 2-D dam break is shown in Fig. 15 with the dimensions of H_w, L_w, H_f and L_f defined as the wall height and width, and the water height and width, respectively. The height of both side walls is set four times higher than the initial water height. In total, 7250 particles are used (80×40 fluid particles, 802 edge particles, 3248 dummy particles). Initially, the particles are regularly distributed with the closest neighbour distance being $1/80H_f$. In terms of SPH parameters, a fourth order of kernel and smoothing length ratio h/dr of 1.3 are again used.

An approximation of the maximum fluid velocity $\bar{u}_{max}$ is estimated from the theory of characteristic curves [20] as

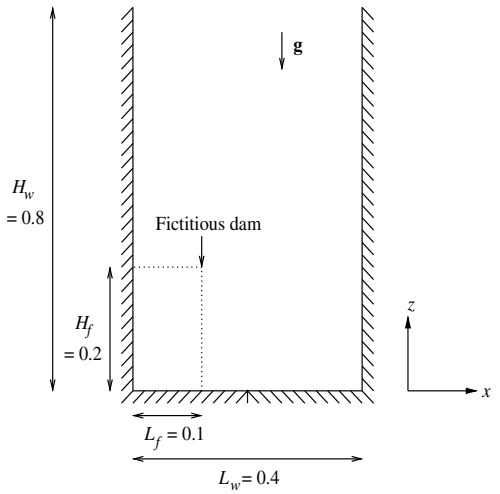

Fig. 15. Configuration of a dam breaking on dry bed (unit: m).

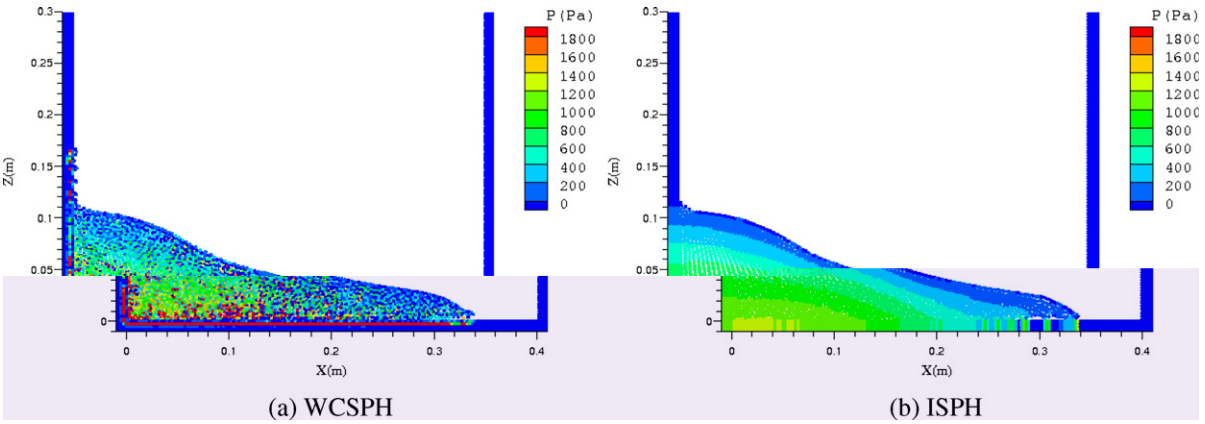

Fig. 16. Dam-breaking case. Pressure pattern at $t = 0.186$ s: (a) WCSPH and (b) ISPH.

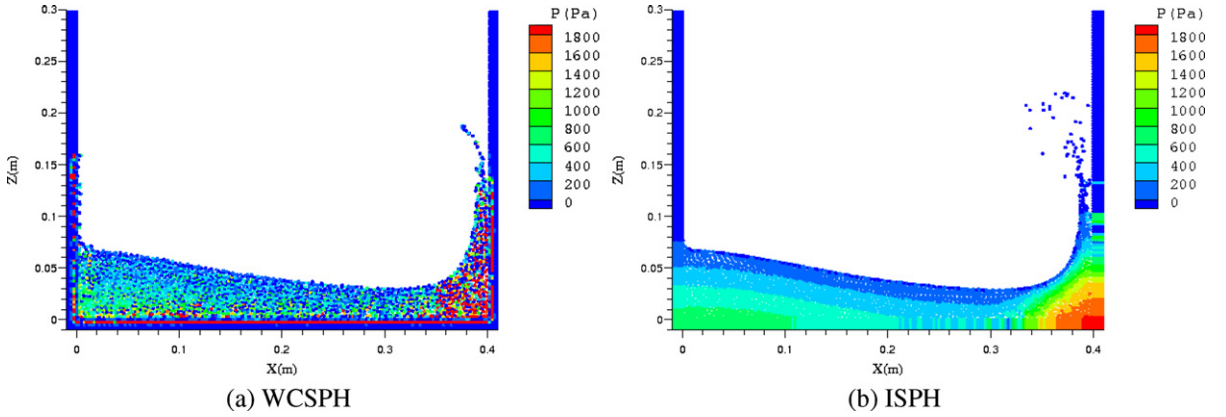

Fig. 17. Dam-breaking case. Pressure pattern at $t = 0.278$ s.

$$\bar{u}_{\max} = 2\sqrt{gH_f} \tag{34}$$

where g and H_f are respectively gravity and initial water height. This gives a maximum fluid velocity is 2.8 m s^{-1} and numerical speed of sound c_0 in WCSPH is set 10 times higher. Initially, pressure for all fluid particles (denoted by p_a) is given by a hydrostatic law:

$$p_a = \rho_a g(H_f - z_a) \tag{35}$$

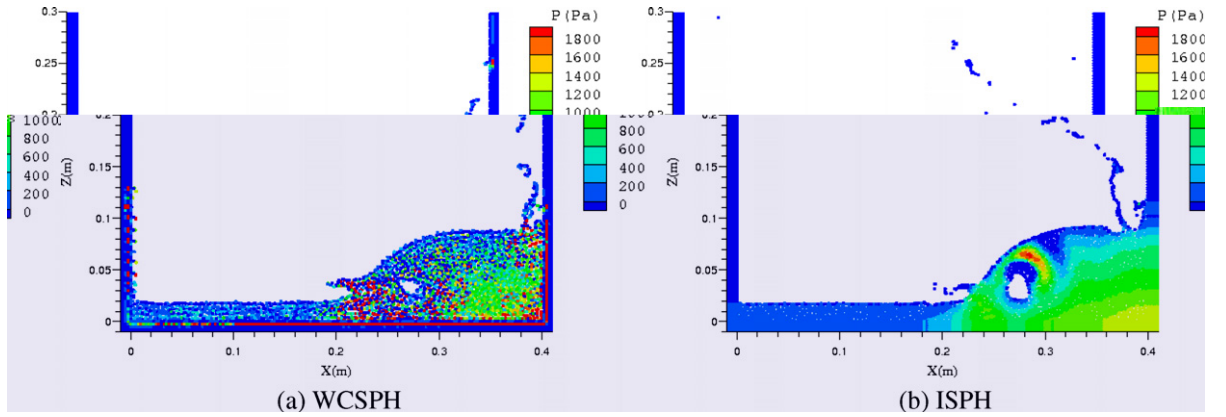

Fig. 18. Dam-breaking case. Pressure pattern at $t = 0.650$ s.

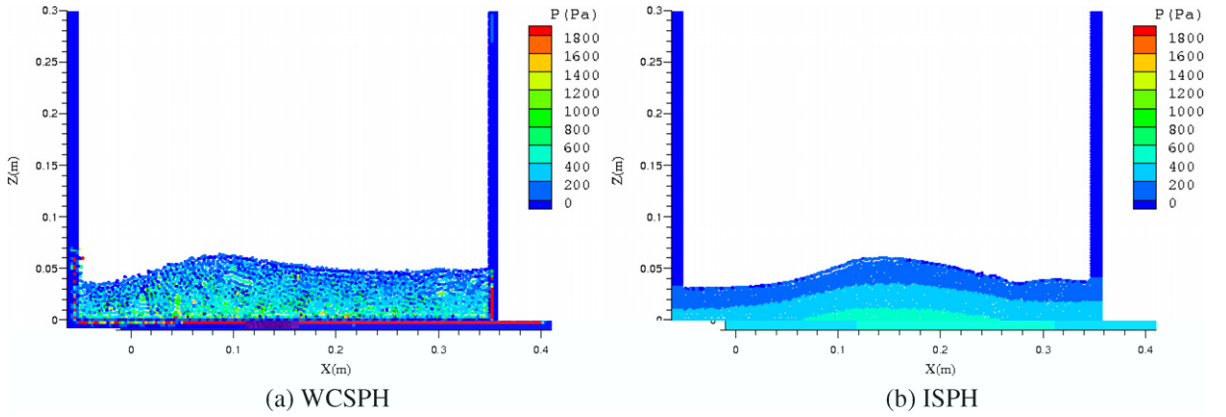

Fig. 19. Dam-breaking case. Pressure pattern at $t = 1.860$ s.

6.2. Results on dry bed

Pressure fields for WCSPH and ISPH are compared at a given time (see from Figs. 16–19). To focus on the fluid field, the side walls are cut at 0.3 m height in the figures. In terms of surface shape, these two approaches show very similar behaviour until the reflection of the wave on the opposite wall, then there are some small differences with more splash in ISPH (Fig. 18), and a slightly different reflected wave speed (Fig. 19). Regarding the pressure fields, again ISPH significantly reduces the pressure noise in comparison with WCSPH.

6.3. Simulation conditions on wet bed

In the experiment reported by Jánosi et al. [9], various water depths d were examined by keeping the dam-break height d_0 as 0.15 m and the gate velocity of 1.5 m s^{-1}. However, in the numerical simulation only one case where the water depth d is 0.018 m was chosen and compared (Fig. 20). The maximum fluid velocity is set as 1.25 m s^{-1}, to give a lower limit to time step without violating the Courant condition. Increasing this velocity had negligible influence in the result (although a smaller time step was needed). In total, 21,805 particles are used (17,805 fluid particles, 792 edge particles, 3208 dummy particles). Initially, the particles are regularly distributed with the closest neighbour distance being dr = 0.002 m. In terms of SPH parameters, a fourth order of kernel and smoothing length ratio h/dr of 1.5 are used. Unlike the previous case, pressure is initially set at zero for all fluid particles.

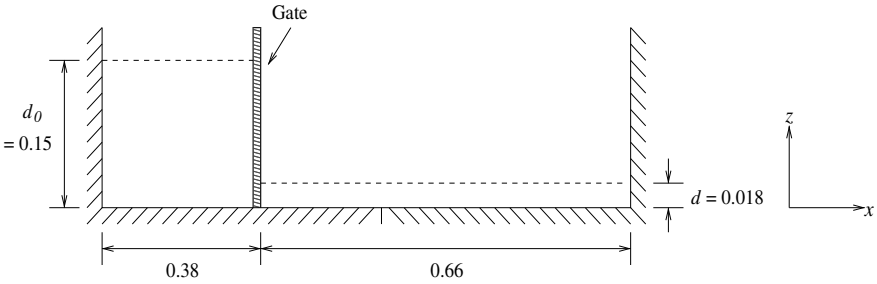

Fig. 20. Configuration of a dam breaking on wet bed (unit: m).

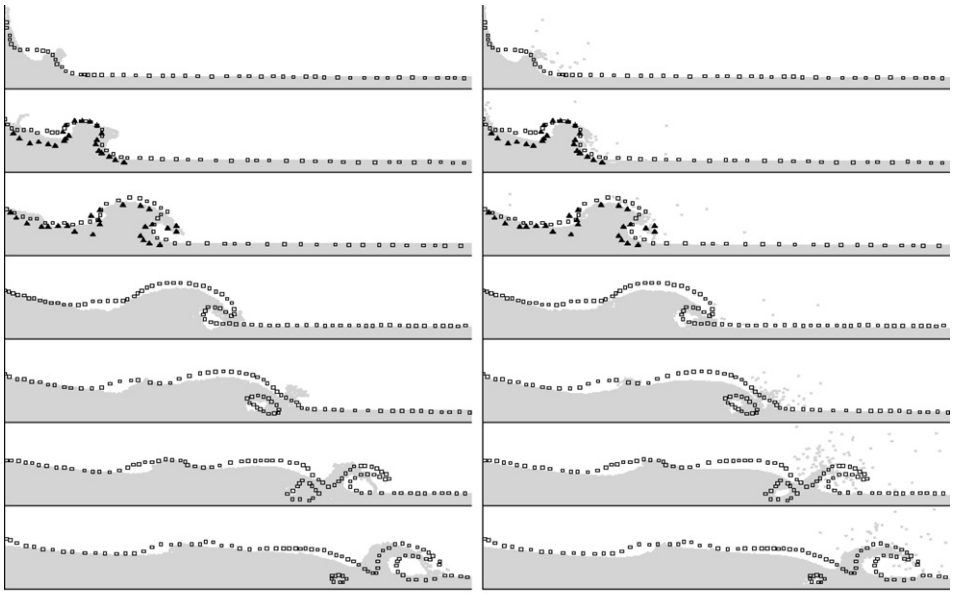

Fig. 21. Free-surface evolution for WCSPH and ISPH. Comparisons of the surface shape with experimental data from Jánosi et al. [9] (□) and Stansby et al. [20] (▲). From top to bottom the physical time is 0.156 s, 0.219 s, 0.281 s, 0.343 s, 0.406 s, 0.468 s and 0.531 s. Note equivalent times for [20] are 0.206 s and 0.28 s.

6.4. Results on wet bed

The results shown in Fig. 21 are mainly to compare the surface shape. The initial stages of surface shapes in WCSPH and ISPH are different from experiment [9] although the initial mushroom shapes were observed and predicted in [20]. With almost instantaneous dam removal, these shapes are also shown in Fig. 21 for earlier times. In [9] the plate is said to be removed with a speed of 1.5 m s^{-1} which would take a time 0.1 s. Due to inertia effects the time will inevitably be longer and this could explain the difference between the experimental results in [9,20]. In general, WCSPH and ISPH show similar patterns of surface shape except there are more splashes and voids in ISPH. The voids in ISPH (the last three figures from the bottom in Fig. 21) are also observed in the experiment. In terms of CPU time, WCSPH takes about 55 min while ISPH does about 15 min. Both methods produce quite realistic representation of the various phenomena: the detaching and breaking front wave which then rebounds as a second breaking wave and enclosing a large void. Both SPH methods show some perturbations at this location. This last example does not allow one to conclude as to whether one or the other solver is superior, but shows that both are equally robust for representation of violent surface motion.

7. Conclusions

In this paper, the 2-D applications of a lid-driven cavity flow, a flow around a bluff body located between two flat plates and a dam-breaking case, have been simulated in order to compare WCSPH and ISPH. Overall, ISPH yields much more reliable results than WCSPH; velocity and pressure fields in particular are smoother in every case. For the lid-driven cavity for instance, although the error shows a first-order scheme convergence rate, on the coarser resolutions ISPH approaches a flow field that is much closer to the exact solution than the WCSPH results which are very noisy and seem to correspond to a much more viscous flow regime. At higher *Re* number and with a finer discretisation, the WCSPH is improved and is closer to ISPH. However, short range and very intense pressure fluctuations produced by WCSPH in the instantaneous fields are so large that they mask the mean pressure variation. This is also generally true for unsteady pressure distributions in the bluff body and dam-break problems, although the surface profiles for the dam-break case were in close agreement. In all cases, the CPU time required by ISPH is shorter, by about a factor of 2–20 depending on the cases.

Further work can be undertaken to improve the ISPH method. Neumann pressure conditions at the wall using dummy particles require further study and comparison with the mirror-particle technique or direct modification of the Laplacian operator matrix as in finite elements. The simulation time could be reduced by purely numerical developments such as pre-conditioning for the linear solver.

Acknowledgement

This work has been funded by EPSRC (Grant GR/S28310).

References

[1] D.S. Balsara, von Neumann stability analysis of smoothed particle hydrodynamics – suggestions for optimal algorithms, J. Comput. Phys. 121 (1995) 357–372.
[2] A.J. Chorin, Numerical solution of the Navier–Stokes equations, Math. Comp. 22 (1968) 745–762.
[3] P.W. Cleary, J.J. Monaghan, Conduction modelling using smoothed particle hydrodynamics, J. Comput. Phys. 148 (1999) 227–264.
[4] S.J. Cummins, M. Rudman, An SPH projection method, J. Comput. Phys. 152 (1999) 584–607.
[5] U. Ghia, K.N. Ghia, C.T. Shin, High-Re solutions for incompressible flow using the Navier–Stokes equations and a multigrid method, J. Comput. Phys. 48 (1982) 387–411.
[6] R.A. Gingold, J.J. Monaghan, Smoothed particle hydrodynamics: theory and application to non-spherical stars, MNRAS 181 (1977) 375.
[7] R. Issa, Numerical assessment of the smoothed particle hydrodynamics gridless method for incompressible flows and its extension to turbulent flows, PhD thesis report, UMIST, 2005.
[8] R. Issa, E.-S. Lee, D. Violeau, D.R. Laurence, Incompressible separated flows simulation with the smoothed particle hydrodynamics gridless method, Int. J. Numer. Methods Fluids 47 (2005) 1101–1106.
[9] I.M. Jánosi, D. Jan, K.G. Szabó, T. Tél, Turbulent drag reduction in dam-break flows, Exp. Fluids 37 (2004) 219–229.
[10] D-H. Kim, K-S. Yang, M. Senda, Large-eddy simulation of turbulent flow past a square cylinder confined in a channel, Comp. Fluids 33 (2004) 81–96.
[11] L.B. Lucy, A numerical approach to the testing of fusion process, Astron. J. 82 (1977) 1013–1024.
[12] J.J. Monaghan, Particle methods for hydrodynamics, Comput. Phys. Rep. 3 (1985) 71.
[13] J.J. Monaghan, Smoothed particle hydrodynamics, Annu. Rev. Astron. Astrophy. 30 (1992) 543–574.
[14] J.J. Monaghan, Simulating free surface flows with SPH, J. Comput. Phys. 110 (1994) 399–406.
[15] J.P. Morris, P.J. Fox, Y. Zhu, Modeling low Reynolds number incompressible flows using SPH, J. Comput. Phys. 136 (1997) 214–226.
[16] S. Nakagawa, K. Nitta, M. Senda, An experimental study on unsteady turbulent near wake of a rectangular cylinder in channel flow, Exp. Fluids 27 (1999) 284–294.
[17] M. Perić, Confidential communication, 2004.
[18] N.J. Quinlan, M. Basa, M. Lastiwka, Truncation error in mesh-free particle methods, Int. J. Numer. Methods Eng. 66 (2006) 2064–2085.
[19] S. Shao, E.Y.M. Lo, Incompressible SPH method for simulating Newtonian and non-Newtonian flows with a free surface, Adv. Water Resour. 26 (2003) 787–800.
[20] P.K. Stansby, A. Chegini, T.C.D. Barnes, The initial stages of dam-break flow, J. Fluid Mech. 374 (1998) 407–424.
[21] R. Temam, Sur l'approximation de la solution des équations de Navier–Stokes par la méthode des pas fractionnaires II, Qrch. Ration. Mech. Anal. 33 (1969) 377–385.
[22] D. Violeau, One and two-equations turbulent closures for smoothed particle hydrodynamics, in: S.-Y. Liong, K.-K. Phoon, V. Babovitch (Eds.), 6th International Conference on Hydroinformatics, EDF R&D, World Scientific Publishing Company, Singapore, 2004.

[23] D. Violeau, User's guide for the SPARTACUS-2D V1P0 code: Lagrangian modelling of 2-dimensional laminar and turbulent flows with SPH method, Technical report, 2004.
[24] D. Violeau, R. Issa, Numerical modelling of complex turbulent free surface flows with the SPH method: an overview, Int. J. Numer. Methods Fluids 53 (2) (2007) 277–304.
[25] H.A. Van Der Vorst, Bi-CGSTAB: A fast and smoothly converging variant of Bi-CG for the solution of nonsymmetric linear systems, S.J. Sci. Stat. Comput. 13 (1992) 631–644.